

The Open University's repository of research publications and other research outputs

Substructure Development and Deformation Twinning Stimulation through Regulating the Processing Path during Multi-Axial Forging of Twinning Induced Plasticity Steel

Journal Item

How to cite:

Akbarian, Shima; Zarei-Hanzaki, Abbas; Abedi, Hamid Reza; Unnikrishnan, Rahul and Moat, Richard (2018). Substructure Development and Deformation Twinning Stimulation through Regulating the Processing Path during Multi-Axial Forging of Twinning Induced Plasticity Steel. *Advanced Engineering Materials*, 20(11), article no. 1800453.

For guidance on citations see [FAQs](#).

© 2018 Wiley-VCH Verlag GmbH Co. KGaA, Weinheim

Version: Accepted Manuscript

Link(s) to article on publisher's website:

<http://dx.doi.org/doi:10.1002/adem.201800453>

Copyright and Moral Rights for the articles on this site are retained by the individual authors and/or other copyright owners. For more information on Open Research Online's data [policy](#) on reuse of materials please consult the policies page.

Substructure development and deformation twinning stimulation through regulating the processing path during multi-axial forging of twinning induced plasticity steel

SH. Akbarian^a, A. Zarei Hanzaki^{a,*}, H. R. Abedi^a, R. Unnikrishnan^b, R.J. Moat^b

^a Hot Deformation & Thermomechanical Processing Laboratory of High Performance Engineering Materials, School of Metallurgy and Materials Engineering, College of Engineering, University of Tehran, Tehran, Iran.

^b School of Engineering and Innovation, STEM, The Open University, Milton Keynes, MK7 6AA, UK

Abstract

Multi-axial forging (MAF) at room temperature was employed to investigate the effects of deformation processing path and the amount of imposed strain on the deformation mechanisms of a twinning-induced plasticity (TWIP) steel. The results indicated that the twin frequency was decreased by applying the 2nd compression ($\sum \epsilon=0.8$), however, an unexpected increase was realized at the end of first MAF pass ($\sum \epsilon=1.2$). This was attributed to the change in strain path and orientation dependence of deformation twinning. The latter is phenomenal considering the previous researches reporting the suppression of twinning at the early stage of deformation ($\epsilon < 0.4$). The same sequence is followed during the second pass of MAF process. Interestingly, the progressive and continues substructure development along with dynamic Hall-Petch effect results from deformation twinning leads to an appreciable grain refinement. The latter is accompanied by the sharp drop of hardening rate in corresponding flow curves. The microtexture analysis indicates the strengthened texture of the 1pass-processed specimens which is weakened at the end of 2 pass due to the recrystallization and increasing the number of texture component. The current work also explores the room temperature mechanical properties of the multi axial forged workpiece through elaborating the miniaturized tensile testing method.

Keywords: TWIP steels; Multi-axial forging; Strain path; Continuous dynamic recrystallization; Twinning

* Corresponding author
E-mail address: zareih@ut.ac.ir (A. Zarei- Hanzaki)
Tel.: +98 21 82084116; fax: +98 21 88006076

1. Introduction

The exceptional strain hardening behavior of commercial twinning induced plasticity (TWIP) steels at room temperature has extensively attracted the industrial interests in recent years ^[1]. Accordingly, numerous systematic studies have been conducted to explore the influence of different deformation parameters, including the magnitude of strain, strain rate and deformation mode on their dominant operating deformation mechanisms ^{[2]-[4]}. The majority of previous researchers believed on the planar nature of the dislocation glide during room temperature deformation of TWIP steels ^{[5][6]}. However, Gutierrez-Urrutia et.al ^[3] reported that the deformation mechanism at the initial stages of straining was accompanied with the formation of dislocation cells and highly dense dislocation configuration; these would act as strong barriers to dislocation glide during further straining thereby resulting in an appreciable strain hardening behavior. Furthermore, at the finishing stages of straining (e.g., final stages during tensile test before fracture), the rate of strain hardening was decreased due to the subordinate capability of the material for further substructure refinement and dislocation trapping. In addition, other researchers have reported ^{[7]-[9]} the feasibility of hardening through progressive substructure development associated with wavy glide (cell formation, refinement, size stabilization and its rotation) during room temperature deformation of duplex low-density steels holding a high SFE of 85 mJ/m². In this regard, Pham et. al. ^[10] reported the ability of dislocation rearrangement from planar to the cellular structure under cyclic loading in low SFE austenitic steels. Another worthy point would be the contribution of deformation twinning. The twin boundaries may gradually reduce the effective glide distance of lattice dislocations and make them effective barriers to dislocation slip; this has been referred to as “dynamical Hall-Petch effect” in the corresponding literatures ^{[1][11]}. However, most of the above investigations, even under the severe

plastic deformation (such as equal-channel angular extrusion (ECAE) ^{[12][13]} and high-pressure torsion (HPT) ^{[14]-[16]}), have only observed deformation twinning suppression in the early stages of processing. In addition, the deformation twinning appeared to be strictly orientation dependent in the course of deformation. Yang et. al ^[17] reported that the twinning could be proceeded rapidly during compressing the material but was suppressed at strains lower than that of the tension mode. These could well represent the significant influence of the strain path on the dislocation configuration, glide characteristics and deformation twinning irrespective of the amount of imposed strain.

Despite the comprehensive wealth of knowledge regarding the room temperature deformation behavior of TWIP steels, there are limited systematic reports on the impacts of deformation processing path on the value and effectiveness of deformation twinning and substructure development. In the present work, an elaborated multi-axial forging (MAF) as a capable severe plastic deformation method has been utilized to study the influence of deformation processing path on the aforementioned microstructural characteristics. This (MAF) well developed severe plastic deformation method is able to provide a set of different strain paths of interest in each deformation cycle and therefore can grant a proper condition for monitoring the gradual microstructural changes and the corresponding flow behavior during the applied sequential compression passes. In addition, the present work was also conducted to examine any new aspects of continuous grain refinement in TWIP steels under different sequential strain paths provided by multi-axial forging (MAF). To this end, the corresponding room temperature mechanical properties of the multi axially forged materials were also evaluated by a miniaturized tensile testing method and the results were comprehensively explained.

2. Material and experimental procedures

2.1. Experimental Material

The experimental steel, chemical composition of which is given in [Table 1](#), was received in as-hot forged condition. The material was annealed at 1100°C for 45 min and then quenched in water to standardize the initial characteristics (e.g., microstructure). The material stacking fault energy (SFE) at room temperature was calculated (~ 35 mJ/m²) based on a sub-regular solution of the proposed thermodynamic model by Grässer [\[18\]\[19\]](#).

2.2. Multi-axial forging procedure

The predetermined cycles of severe plastic deformation at room temperature were applied using a multi-axial forging (MAF) rig. The latter was consisted of forging dies with a rectangular shape constraint with the dimension of 8mm×12mm. The corresponding workpieces with initial dimensions of 8mm×8mm×12mm were extracted from the annealed material by electro discharge machining (EDM) method. The predetermined MAF cycles were carried out using a GOTECH AL7000 universal testing machine under a constant stroke speed of 1 mm/min. The schematic step-by-step illustration of the applied MAF process is depicted in [Fig. 1](#). During the first step, the workpiece is compressed down to a 33% reduction in height, thereby imparting effective plastic strain of 0.4 normal to the C plane. During this step, the deformation normal to the A plane is constrained by channel die, whereas the material is free to undergo tensile deformation normal to the B plane. In the next step, the compressed workpiece is placed in the die cavity after 90° rotating, thus the pressing direction (PD), constrained direction (CD) and flow direction (FD) are normal to the A, B and C planes, respectively. Finally, during the last pressing step of the first MAF pass, the workpiece is compressively deformed along the A plane

normal direction and the total effective plastic strain imparted after these three steps (1 MAF pass) in orthogonal directions is 1.2. The experimented material is subjected to the deformation up to 3 MAF cycles (passes) equivalent to the total logarithmic plastic strain of 3.6.

2.3. EBSD characterization

The microstructural analysis was performed in the regions at the center of X- shape flow form of the processed workpieces on the plane containing the final processing axis direction using electron back-scattered diffraction (EBSD) method. The workpiece of interest were mechanically polished followed by electro-polished at 12°C for 30 seconds in a solution of 5 Vol.% of perchloric acid, 15 Vol.% of acetic acid and 80 Vol.% ethanol at an operating voltage of 32 V. The electron backscatter diffraction (EBSD) analysis were performed using a Zeiss Supra 55VP, equipped with a field emission gun (FE-SEM) and with a Nordlys EBSD detector. The corresponding EBSD maps were generated using a step size of 0.2 μm . The data acquisition and post processing were performed using both the HKL Channel 5 and Aztec software including the careful removal followed by noise reduction and the application of the edge-preserving modified Kuwahara filter routine for the orientation averaging ^[20]. The latter routine was based on a 7×7 pixel grid, which would enhance the precision of misorientation detection to below 0.5 deg.

The EBSD IPF map of the initial microstructure is depicted in **Fig. 2a**. As is seen, the microstructure is consisted of equiaxed grains holding a random texture. The corresponding grain boundary analysis reveals a large fraction of annealing twins (**Fig. 2b**). The mean grain sizes with and without consideration of the twin boundaries are 153 ± 1 and $240 \pm 2 \mu\text{m}$, respectively.

2.4. Mechanical tests

In order to evaluate the flow behavior of the processed materials, a miniaturized tensile testing technique was employed. The tensile specimens holding dimensions of 1.8 mm width, 1 mm thickness, and 5 mm gauge length were machined perpendicular to the final processing direction. The tensile tests were carried out at room temperature using SANTAM testing machine under the initial strain rate of 0.001s^{-1} .

3. Results and discussion

3.1. Flow behavior during MAF

The variations of the true stress vs. accumulative strain ($\sum\varepsilon$) during multi axial forging is plotted in [Fig. 3](#). The general shape of the flow curves, which is shown by the dashed line, suggests that the rapid work hardening initiates from the early stage of straining and continued up to $\sum\varepsilon=1.2$. In contrast, at higher strain levels the hardening rate is decreased and reaches to a steady state region. Such behavior has been previously reported by Sakai et al. [\[21\]](#) during the high temperature MAF of ferritic stainless steels possessing high SFE values and attributed to the activation of recovery-controlled dynamic processes. Miura et al. [\[22\]](#) and Belyakov et al. [\[23\]](#) also reported a similar steady-state flow behavior of austenitic stainless steels during room temperature MAF at imposed strains above 1. They proposed that these effects could be induced by balancing of strengthening due to the grain refinement (results from twin fragmentation) and softening due to the dynamic recovery. In the present work, however, the flow stress during the

second pass of MAF is accompanied by work softening, which may be well considered as the activation of new emerging mechanisms. In order to justify this speculation, the microstructure of the specimen processed under different accumulative strains were precisely examined.

3.2. Substructure development

The deformed microstructures at different accumulative strain levels were analyzed to evaluate the capability of substructure development and deformation twinning during MAF process. The grain boundaries in the microstructures deformed up to accumulative strains of 0.4, 0.8 (corresponding to the 1st and 2nd compression steps), 1.2 and 2.4 (corresponding to the 1st and 2nd MAF passes) are presented by EBSD boundary maps in [Fig. 4](#). The twin maps are also superimposed on deformed microstructures up to different strain levels. The $\Sigma 3$ twin boundaries with straight-sided bands that run across the grains, are identified as 60° rotation around a $\langle 111 \rangle$ axis and highlighted in red. The rest of the high angle boundaries are presented in black. The boundary development was also analyzed quantitatively by considering the misorientation angle distributions between neighboring grains/subgrains ([Fig. 5](#)). After the 1st compression, a large fraction of both sub-boundaries (generally ranging between 0 and 5°) and deformation twins are observed within the initial grains ([Fig. 4a](#)). Accordingly, the hardening behavior at this strain level may be related to two parallel strengthening mechanisms: (i) the dislocation substructures, which consist of dislocation cells (DCs) and high dense dislocation walls (HDDW), and (ii) the deformation twins. Apparently, the dislocation arrangements in DC and HDDW can act as effective obstacles against dislocation motion. This form of substructure hardening in TWIP steels has been already reported by Raabe et.al [\[3\]](#). The deformation twinning may contribute to the strain hardening as a result of the “dynamic hall-Petch effect” [\[1\]\[11\]](#). The boundary map in

Fig. 4a reveals that the twin boundaries could cut through the existing dislocation substructure. The twin boundaries are able to act as strong obstacles to dislocation motion, serving as efficient sites for dislocation accumulation similar to the high angle grain boundaries. This effect has been reported as the strengthening mechanism of FCC metals prone to form deformation twins [24].

At the end of the 2nd compression (**Fig. 4b**), the frequency of sub-boundaries and the magnitude of their misorientations are significantly increased. The quantitative analysis (**Fig. 5b**) reveals that most of the sub-boundaries are misoriented in the range of 5-15°. In contrast, the frequency of twin boundaries is decreased as deformation proceeds. The latter may be explained considering the intensified substructure development along with distortion of twin boundaries. In the latter, the twin boundaries have lost their coherency and deviate from $\Sigma 3$ -coincidence relationship in some regions. It is believed that the interacted dislocations are dissociated into the boundary structure, thus a relative rotation between the lattices and twins may be taken place and this in turn would result in the progressive deviation from $\Sigma 3$ -coincidence relationship. This effect has been well discussed previously in the case of TWIP steel under cold rolling where the distortion process induced by twin-slip interactions [25]. The main portion of work hardening (**Fig. 3b**) at this strain level ($\Sigma \varepsilon=0.8$) is considered to be the substructure development.

The high-resolution EBSD grain boundary map of the microstructure after completion of the first MAF pass at $\Sigma \varepsilon=1.2$ is depicted in **Fig. 4c**. Surprisingly, the frequency of deformation twins is significantly increased. In fact, the material flow during MAF is affected by the applied strain path. This can be related to the twofold material flow during each compression. To this end, the center of the workpiece experiences compression mode while a tension one is practiced at the two other sides along with corresponding flow direction. Therefore, some of the twin boundaries (TBs) were formed by 1st compression, but the material experiences an opposite

deformation mode during next compression thereby resulting in distortion process. Therefore, the twin frequency increment by the 3rd compression appears to be reasonable. It is worth noting that the incremental trend of sub-boundary formation is reduced to lower values but its fraction is still high. Therefore, deformation twinning and substructure development both contribute in strain hardening during the 3rd compression. It is worth mentioning that the previous works regarding the deformation behavior of TWIP steels through cold rolling [26]-[28], high pressure torsion [15][16] and equi-channel angular pressing [12] all reported the suppression of twinning at the early stage of processing; these are summarized in **Table. 2**.

As is reported in **Table 2**, during conventional rolling the dislocation slip accommodates the strain at lower strains and at higher strains twinning becomes the predominant deformation mechanism. According to the previous researches the deformation twinning would be suppressed at 60% reduction during rolling and the further strains are accommodated by shear bands without any contribution of twinning and slip [26]-[28]. The deformation mechanism in severe plastic deformation processes [12][15][16][29][30] such as HPT is quite different from rolling condition. The deformation twinning is suppressed at ¼ turn of the first pass. All the above mentioned works have been conducted through on one deformation path, deformation twins suppressed at the early stages with no chance of progressive dislocation slip contribution. In contrast, the present results (fact and figures) approve the contribution of twinning (further twin boundaries) with substructure development in strain hardening behavior of the material even at significantly larger strains. The latter put emphasize on the significant influence of the change in strain path on capability of coupling the deformation twinning with substructure development during room temperature deformation of the experimented steel.

Fig. 4c also shows some twin-like parallel bands which may not index as twin boundaries and occur at $\sim 42^\circ$ to the final forging axis. These bands correspond to narrow regions of intense shear that occur independently of the grain structure. It is suggested that the rearrangement of twin lamellae at lower deformation stages is followed by macro shear band-like formation by moderate strains. The latter can be clearly observed in the high resolution EBSD grain boundary map of the microstructure deformed up to the true strain of 1.2 (**Fig. 4c**). The similar characters regarding the feasibility of shear band formation have been previously observed at relatively high reduction (strain of about 80%) during cold rolling of TWIP steels ^[27].

The same consequences are repeated during the second pass of MAF processing. The observed steady state flow and the sharp drop of hardening rate during the second pass (**Fig. 3**) are attributed to the extended recovery and the occurrence of partially continuous dynamic recrystallization. Such behavior has been previously reported during high temperature deformation of twinning induced plasticity steels possessing low stacking fault energy values ^{[31]-[34]}, the details of which will be discussed in the next section.

3.3. Grain refinement Mechanisms

The low angle boundaries in **Fig. 4** are classified into three categories, denoting by the ranges of $0.7^\circ < \Theta < 2^\circ$ (class I), $2^\circ < \Theta < 5^\circ$ (class II), and $5^\circ < \Theta < 15^\circ$ (class III) and highlighted by the gray, indigo and purple lines, respectively. The subgrains formation is clearly visible owing to the considerable dislocation dissociation into the developed low angle boundaries which result in further increase of the sub-boundaries misorientation up to $5\text{-}15^\circ$ after 2nd compression (**Fig. 5a, b**). As is realized in **Fig. 5d**, due to the subgrains rotation the sub-boundaries population is significantly decreased and conversely the fraction of high angle boundaries increases at the end of 2nd MAF passes and consequently the formation of recrystallized grains are observed.

According to the literatures ^{[35][36]}, this may be considered as strong indication of dynamic recrystallization. In this regard, grain average misorientation (GAM) maps are employed to set apart between deformed and recrystallized grains. (**Fig.6a, b**). It is calculated by averaging the misorientations (angles) between all neighboring pairs of points in the selected grains ^{[37][38]}. The results indicate that the recrystallized grains (blue grains), indicated by black arrows, reveal a lower dislocation density compared with deformed ones. Recrystallization is mainly initiated within the shear band like regions (**Fig.6a**) and then further proceeds at higher imposed strains (**Fig.6b**). As is observed in corresponding kernel average misorientation (KAM) map (**Fig.6c**), the nucleated grains are limited to the regions that experienced the highest distortion (localized flow regions). These are the most favorable regions for recrystallization activation due to the necessities of decreasing the high absorbed energy in the deformed microstructure. In order to well trace the recrystallized regions, the boundary map is superimposed on KAM in **Fig. 6d**. The recrystallized regions are completely conforming to the lowest kernel average and bounded with high angle boundaries. The selected area in **Fig. 4c** (region A) is further analyzed to clearly rationalize the grain refinement mechanism. The misorientation profile along line 1 in **Fig. 7a, and b** indicates the presence of high angle boundaries and the occurrence partially recrystallization even at lower imposed strains. It is worth mentioning that some original grains are fragmented to smaller domains due to the activation of secondary twinning with different variants. These are indexed as highly deformed grains (containing higher dislocation density) and are bounded by twin boundaries (**Fig. 6b, d**). In order to give a better insight to the grain refinement mechanism a schematic of the deformed microstructures evolved during MAF process is presented in **Fig. 8**. In general, there are two different grain refinement mechanisms resulted from (i) dynamic recrystallization and (ii) twin fragmentation. Firstly, the high density

of dislocations arrays holding small misorientations (0-5°) is formed within the initial grains at the 1st compression. Subsequently, in 2nd compression by increase in the sub-boundaries misorientations (5-15°) the substructure is developed and the grains are partitioned by subgrains. The subgrains formed at this stage were rotated in shear band like regions and causes subsequent partially continuous dynamic recrystallization. The activation of deformation twins is also traced within the deformed microstructures simultaneously, the fraction of which increases by increasing imposed strain. At the end of first pass, the grains are effectively subdivided by multi-variant deformation twins.

3.4. Microtexture

The EBSD IPF maps from pressing direction (PD) of deformed microstructure up to one and two MAF passes are given in **Fig. 9a, b**. The recrystallized grains which are preferentially formed within the shear band like regions follow completely different microtexture with respect to the parent grains the corresponding higher magnification of the affected area of shear band like regions has been presented in the inset in **Fig. 9a**. The latter is completely consistent with the previous reported results regarding the local texture effect of continuous dynamic recrystallization ^[9]. This is further analyzed through plotting {111} pole figure of the material processed through MAF, as are presented in **Fig. 10a-c**. As is expected, the recrystallized texture (**Fig.10a, c**) appears to be different from the deformation texture (**Fig.10b**). At initial condition the texture intensity is relatively low identifying random texture, but is fairly increased due to intensifying preferential texture formation by increasing the accumulative strain up to $\sum \varepsilon = 1.2$, and then is again decreased at the higher strains. Due to the occurrence of continuous recrystallization the variation of grains orientation has been increased in second pass as shown in **Fig.9b**. In order to well clarify the observed evolution, the microtexture analysis by means of

orientation distribution functions (ODF) is performed. **Fig. 10e-g** demonstrates the texture components for initial and MAFed specimens. As is seen in **Fig. 10e**, initial texture represent the random distribution of the Goss $\{110\} \langle 001 \rangle$, the Brass $\{110\} \langle 112 \rangle$ and the Copper $\{112\} \langle 111 \rangle$ components which is typical for hot deformed face-centered cubic (FCC) metals [24][39]-[41]. As is seen in **Fig. 10f**, after one MAF pass the initial texture components distributions are reassembled to the new deformation texture. The most of researches on the deformation textures of low SFE TWIP steels subjected to the cold working, reported the formation of specified fibers texture [26][28]. However, the new fiber texture in the $\varphi_2 = 45^\circ$ ODF section is obtained after one MAF pass which is formed by the high intensity of the E $\{111\} \langle 011 \rangle$ and the Cube $\{001\} \langle 100 \rangle$ components. The appearance of E component in the present study was also reported for high Mn steel subjected to the cold rolling [28][42][43]. Haase et.al [42] explained that a γ -fiber consisting of the E $\{111\} \langle 011 \rangle$ and F $\{111\} \langle 112 \rangle$ components developed due to the expense of CuT component which reflected by further deformation twinning in Cu-oriented grains. However, in this work at the first pass CuT component couldn't appear due to the high amount of strain. They reported that the formation of E+F components at the 70-80% rolling reduction results from shear bands formation [42][43]. Therefore, it can be concluded that the appearance of E component is represent the formation of shear band like regions at this stage in **Fig. 9a**. It should be emphasized that the formation of Cube component has been recognized as a consequence of recrystallization in the case of low SFE austenitic steels [44]-[46]. In the present work the formation of Cube component is obvious in $\varphi_2 = 0^\circ$ ODF section (**Fig. 10f**) which is attributed to the beginning of recrystallization at the end of one MAF pass. Further at the end of two MAF passes (**Fig. 10d**) the texture weakening occurs by destruction of the aforementioned new fiber texture. Indeed the number of texture components increases due to the occurrence of

continuous recrystallization (**Fig. 9b**) but the intensity of these components consisting of Goss, Brass, Copper and Rotated-Goss are decreased to some extent. As mentioned above such recrystallization texture formation is attributed to the activation of restoration process in hot deformed conditions [42][44][45]. As was discussed in section 3.3, the gradual formation of HABs resulted in continuous recrystallization at the second MAF passes. Therefore, the occurrence of recrystallization may well explain the random texture development. In addition the formation of the Rotated-Goss component $\{011\} \langle 011 \rangle$ is justified by the persistent formation of deformation twinning at this stage [28][40][41]. Therefore, the presence of the random texture resulting in the high efficiency of present TWIP steel for accommodating further strains through the sequential compressions. This is justified considering the fact that the Rotated-Goss component results in hardening and the developed initial texture may soften the deformed microstructure and increase the work hardening capacity. This may describe the observed steady state flow during MAF processes (**Fig. 3**).

3. 4. Mechanical properties

The room temperature tensile flow curves of the processed specimens are presented in **Fig. 11a**. The relatively low yield strength (YS= 209.69 MPa) and high ductility (55%) of experimented material is significantly influenced through imposing MAF process. The details are given in **Fig. 11b** and summarized in **Table. 3**. All of the changes in strengthening parameters and ductility values seem to be reasonably similar to previous reports regarding severe plastic deformation methods [15][28][30][47]. Interestingly, the elongation to fracture of the specimen processed through 2-pass remains relatively constant or even slightly increases compared to 1pass processed specimens. This is completely in agreement with formation of fine recrystallized

grains at the end of 2-pass process. These relatively dislocation free grains can accompany strain during subsequent tensile deformation which in turn increases of hardening capability of the material.

Coming to the point, such a room temperature grain refinement mechanism has not been regularly reported in the case of TWIP steels, due to the unlikeliness of substructure development [48]. However, there are some reports regarding dynamic recrystallization by means of dislocation driven fragmentation or complex dislocation and grain boundary activities at relatively higher temperature of 300°C and at higher imposed strain levels (Table. 2) [30][47][49][50]. Moreover, austenitic steels, which undergo martensite transformation rather than twins, were found to be incapable of room temperature recrystallization even in the course of multi-axial forging [50]. In fact, the martensitic transformation was not significantly affected through the change in strain path. In contrast, in the present case the capability of substructure development and dislocation rearrangement could be increased due to changing the strain path, which might finally result in activation of continuous dynamic recrystallization. In this regard, any change in dislocation configuration should be discussed through precise transmission electron microscopy and would be addressed in future works.

Conclusion

The effect of sequentially changing the deformation path on the deformation mechanism of Fe- 29.1Mn- 0.039C- 2.4Al- 0.3Si twinning-induced plasticity steel was precisely studied. The obtained results can be summarized as follows:

- The substructure development and deformation twinning may contribute in strain hardening of the experimented steel at various trial of multi-axial forging. It was found

that the extent of each mechanism may be significantly affected through the specified deformation path.

- At the end of 2nd compression ($\sum\varepsilon=0.8$), the frequency of deformation twins was considerably decreases. This was explained by progressive deviating of special twin boundaries from $\Sigma 3$ -coincidence relationship.
- At the end of 1 pass ($\sum\varepsilon=1.2$), the frequency of deformation twins increases unexpectedly due to the positive effect of strain path change. Accordingly, deformation twinning and substructures development both incessantly contributed in room temperature strain hardening of the experimental steel. This was led to appreciable grain refinement at high imposed strains.
- Room temperature continuous dynamic recrystallization was achieved by the formation of new fiber texture consisting E and Cube components at one MAF pass which further destructed to the randomized texture (Goss, Brass, Copper and Rotated-Goss components) after the end of second MAF passes.
- Owing to the formation of the well-defined dislocation free grains via partially continuous recrystallization the hardening capability of the processed materials was increased.

References

- [1] B.C. De Cooman, O. Kwon, K. Chin, *Mater. Sci. Technol* **2016**, 28, 513.
- [2] P. Yang, Q. Xie, L. Meng, H. Ding, Z. Tang, *Scr. Mater* **2006**, 55, 629.
- [3] I. Gutierrez-Urrutia, D. Raabe, *Acta Mater* **2011**, 59, 6449.

- [4] D. Barbier, *Mater. Sci. Eng. A* **2009**, *500*, 196.
- [5] I. Gutierrez-Urrutia, D. Raabe, *Acta Mater.* **2012**, *60*, 579.
- [6] B. Ma, C. Li, J. Zheng, Y. Song, Y. Han, *Mater. Des.* **2016**, *92*, 313.
- [7] H.R. Abedi, A. Zarei Hanzaki, N. Haghdadi, P.D. Hodgson, *Scr. Mater.* **2017**, *128*, 69.
- [8] H.R. Abedi, A. Zarei Hanzaki, K. Ou, C. Yu, *Mater. Des.* **2017**, *116*, 472.
- [9] H.R. Abedi, A. Zarei Hanzaki, Z. Liu, R. Xin, N. Haghdadi, P.D. Hodgson, *Mater. Des.* **2016**, *114*, 55.
- [10] M.S. Pham, C. Solenthaler, K.G.F. Janssens, S.R. Holdsworth, *Mater. Sci. Eng. A* **2011**, *528*, 3261.
- [11] L. Mosecker, A. Schwedt, W. Bleck, *Metall. Mater. Trans. A* **2012**, *43*, 1688.
- [12] E. Bagherpour, M. Reihanian, R. Ebrahimi, *Mater. Des.* **2012**, *36*, 391.
- [13] S. Li, X. Li, L. Yang, *Acta Mater.* **2013**, *61*, 4398.
- [14] J.G. Kim, N.A. Enikeev, M.M. Abramova, B.H. Park, R.Z. Valiev, H.S. Kim, *Mater. Sci. Eng. A* **2017**, *682*, 164.
- [15] M.S. Matoso, R.B. Figueiredo, M. Kawasaki, D.B. Santos, T.G. Langdon, *Scr. Mater.* **2012**, *67*, 649.
- [16] M.M. Abramova, N.A. Enikeev, J.G. Kim, R.Z. Valiev, M. V Karavaeva, H.S. Kim, *Mater. Lett.* **2016**, *166*, 321.
- [17] L. Meng, P. Yang, Q. Xie, H. Ding, Z. Tang, *Scr. Mater.* **2007**, *56*, 931.
- [18] O. Grässel, L. Krüger, G. Frommeyer, L.W. Meyer, *Int. J. Plast.* **2000**, *16*, 1391.
- [19] S. Allain, J.P. Chateau, O. Bouaziz, S. Migot, N. Guelton, *Mater. Sci. Eng. A* **2004**, *387–389*, 158.
- [20] F.J. Humphreys, P.S. Bate, P.J. Hurley, *J. Microsc. (Oxford, U. K.)* **2001**, *201*, 50.
- [21] T. Sakai, A. Belyakov, H. Miura, *Metall. Mater. Trans. A* **2008**, *39*, 2206.

- [22] Y. Nakao, H. Miura, *Mater. Sci. Eng. A* **2011**, 528, 1310.
- [23] M. Tikhonova, I. Shakhova, R. Kaibyshev, A. Belyakov, *Mater. Sci. Forum.* **2017**, 879, 1957.
- [24] L. Bracke, K. Verbeken, L. Kestens, J. Penning, *Acta Mater.* **2009**, 57, 1512.
- [25] N.K. Tewary, S.K. Ghosh, S. Bera, D. Chakrabarti, S. Chatterjee, *Mater. Sci. Eng. A* **2014**, 615, 405.
- [26] N. Eftekhari, A. Zarei-hanzaki, A. Shamsolhodaei, A. Helbert, T. Baudin, *Adv. Eng. Mater.* **2018**, 1700928, 1.
- [27] P. Kusakin, A. Belyakov, C. Haase, R. Kaibyshev, D.A. Molodov, *Mater. Sci. Eng. A* **2014**, 617, 52.
- [28] M. Klimova, S. Zhrebtssov, N. Stepanov, G. Salishchev, C. Haase, D.A. Molodov, *Mater. Charact.* **2017**, 132, 20.
- [29] X.H.An, Q.Y.Lin, G.Sha, M.X.Huang, S.P. Ringer, Y.T. Zhu, X.Z. Liao, *Acta Mater* **2016**, 109, 300.
- [30] I.B. Timokhina, A. Medvedev, R. Lapovok, *Mater. Sci. Eng. A* **2014**, 593, 163.
- [31] A. Takayama, X. Yang, H. Miura, T. Sakai, *Mater. Sci. Eng. A* **2008**, 478, 221.
- [32] M. Eskandari, A. Zarei-hanzaki, A. Marandi, *Mater. Des.* **2012**, 39, 279.
- [33] J. Hajkazemi, A. Zarei-hanzaki, M. Sabet, S. Khoddam, *Mater. Sci. Eng. A.* **2011**, 530, 233.
- [34] A.R. Khalesian, A. Zarei-hanzaki, H.R. Abedi, F. Pilehva, *Mater. Sci. Eng. A.* **2013**, 596, 200.
- [35] A. Belyakov, T. Sakai, H. Miura, R. Kaibyshev, K. Tsuzaki, *Acta Mater.* **2002**, 50, 1547.
- [36] S. Gourdet, F. Montheillet, *Acta Mater.* **2003**, 51, 2685.
- [37] S. Mitsche, P. Poelt, C. Sommitsch, *J. Microsc. (Oxford, U. K.)* **2007**, 227, 267.
- [38] S.K. Sahoo, V.D. Hiwarkar, I. Samajdar, P. Pant, D. Srivastav, R. Tewari, G.K. Dey, S.

- Banerjee, *Scr. Mater.* **2007**, *56*, 963.
- [39] M.P. Butrón-Guillén, J.J. Jonas, R.K. Ray, *Acta. Mater.* **1994**, *42*, 3615.
- [40] J.A. Jiménez, G. Frommeyer, *Mater. Charact.* **2010**, *61*, 221.
- [41] D. Barbier, N. Gey, S. Allain, N. Bozzolo, M. Humbert, *Mater. Sci. Eng. A* **2009**, *500*, 196.
- [42] C. Haase, L.A. Barrales-mora, F. Roters, D.A. Molodov, *Acta. Mater* **2014**, *80*, 327.
- [43] S. Vercammen, B. Blanpain, B.C. De Cooman, P. Wollants, *Acta Mater.* **2004**, *52*, 2005.
- [44] Y.H. Sha, C. Sun, F. Zhang, D. Patel, X. Chen, S.R. Kalidindi, L. Zuo, *Acta Mater.* **2014**, *76*, 106.
- [45] D. Raabe, *Mater. Sci. Technol.* **1995**, *11*, 461.
- [46] D. Raabe, *Acta. Mater* **1997**, *45*, 1137.
- [47] C. Haase, O. Kremer, W. Hu, T. Ingendahl, R. Lapovok, D.A. Molodov, *Acta Mater.* **2016**, *107*, 239.
- [48] B.C. De Cooman, Y. Estrin, S. Kyu, *Acta Mater.* **2017**, *xxx*, 1.
- [49] L. Wang, J.A. Benito, J. Calvo, J.M. Cabrera, *J. Mater. Sci.* **2017**, *52*, 6288.
- [50] S.S.S. Kumar, M. Vasanth, V. Singh, P. Ghosal, T. Raghu, *J. Alloys Compd.* **2017**, *699*, 1036.

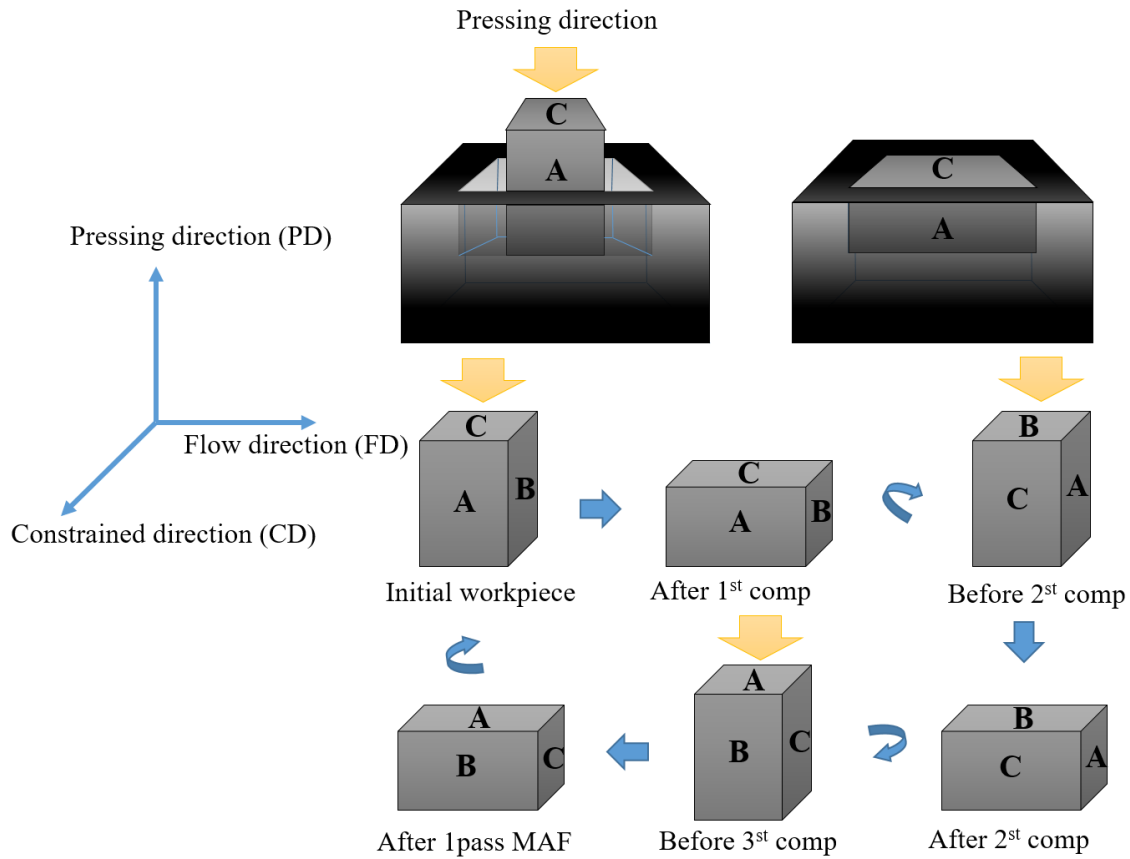


Fig. 1. The schematic representation of the applied multi-axial forging (MAF) method.

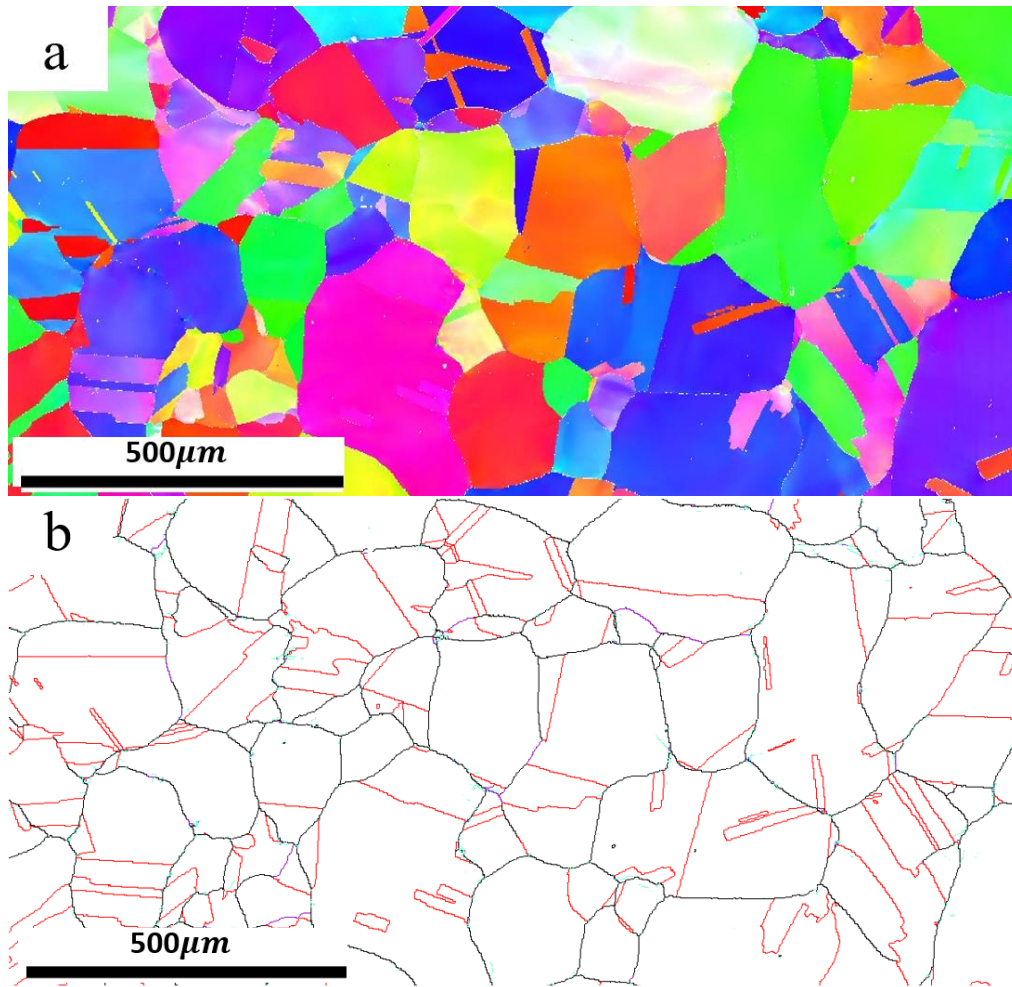


Fig. 2. (a) The inverse pole figure (IPF), and (b) the annealing twin map of the initial microstructure.

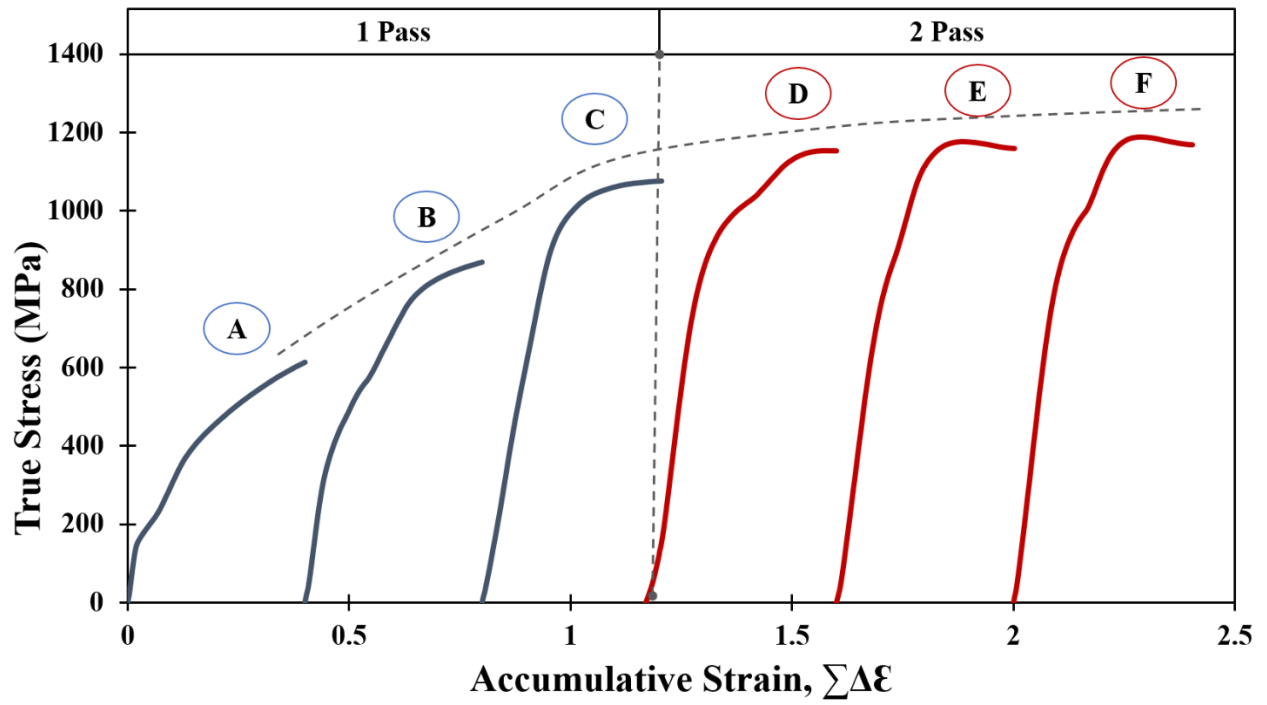


Fig. 3. The variation of true stress with cumulative strain during MAF of the experimental high Mn TWIP steel at room temperature.

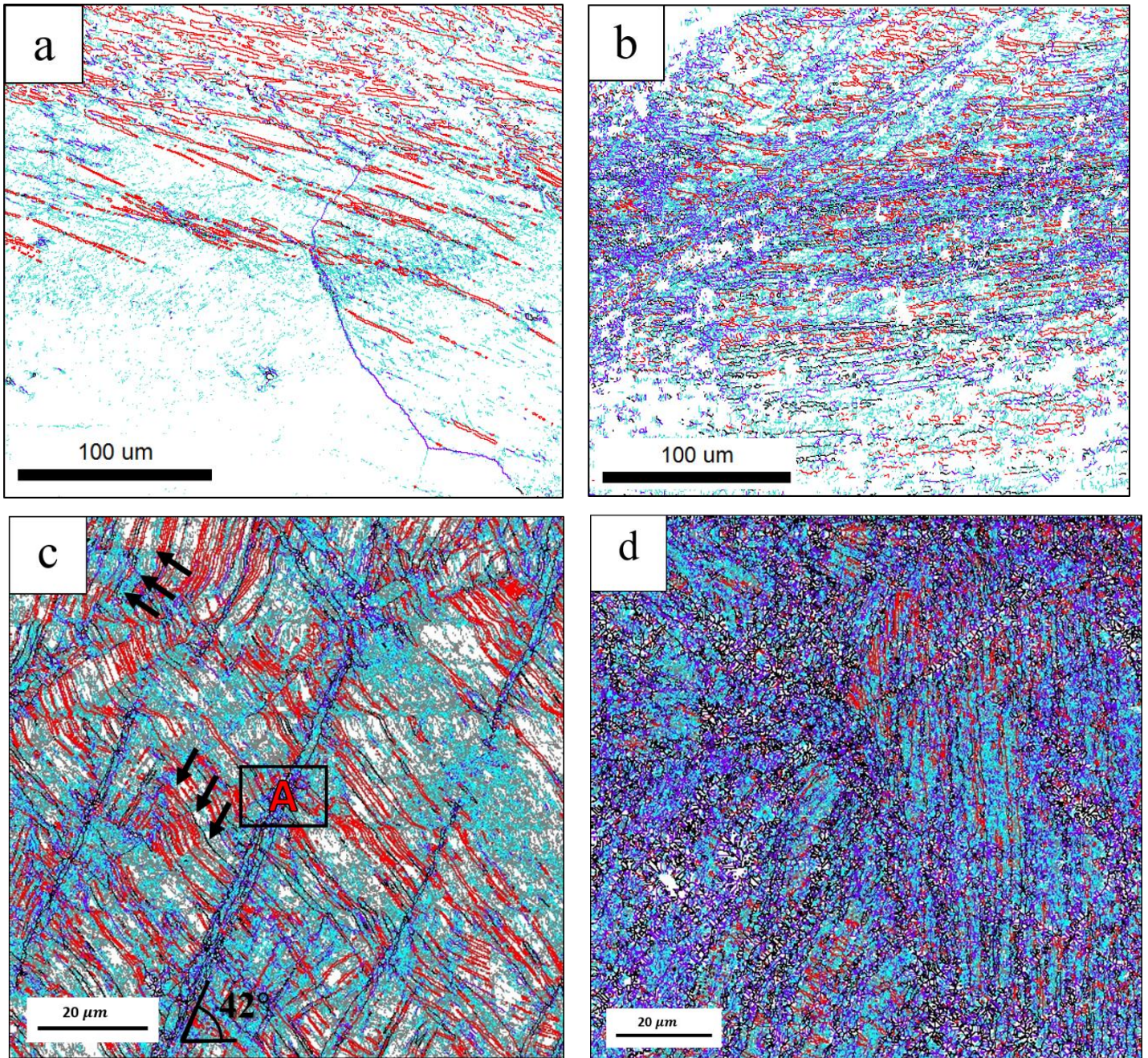


Fig.4. The EBSD orientation maps illustrating the austenite grain boundaries at the interrupted strain of (a) 0.4, (b) 0.8, (c) 1.2 (1st MAF pass), and (d) 2.4 (2nd MAF pass). Gray, indigo, and purple lines holding misorientations in the range of $0.7^\circ < \Theta < 2^\circ$, $2^\circ < \Theta < 5^\circ$, and $5^\circ < \Theta < 15^\circ$, respectively. The black lines represent the high-angle grain boundaries having misorientation of $>15^\circ$. The red lines are $\Sigma 3$.

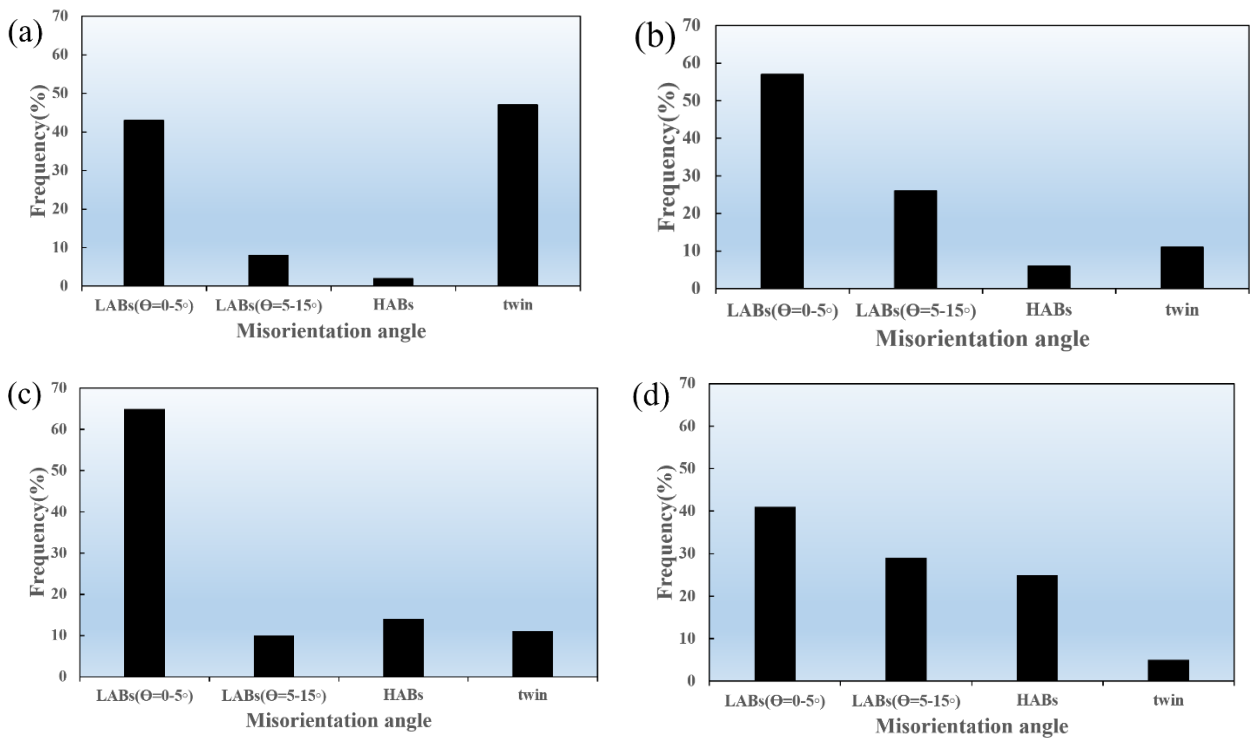


Fig. 5. The misorientation angle distributions in the microstructures of the workpieces deformed under different conditions of (a) $\sum \epsilon = 0.4$, (b) $\sum \epsilon = 0.8$, (c) $\sum \epsilon = 1.2$, and (d) $\sum \epsilon = 2.4$.

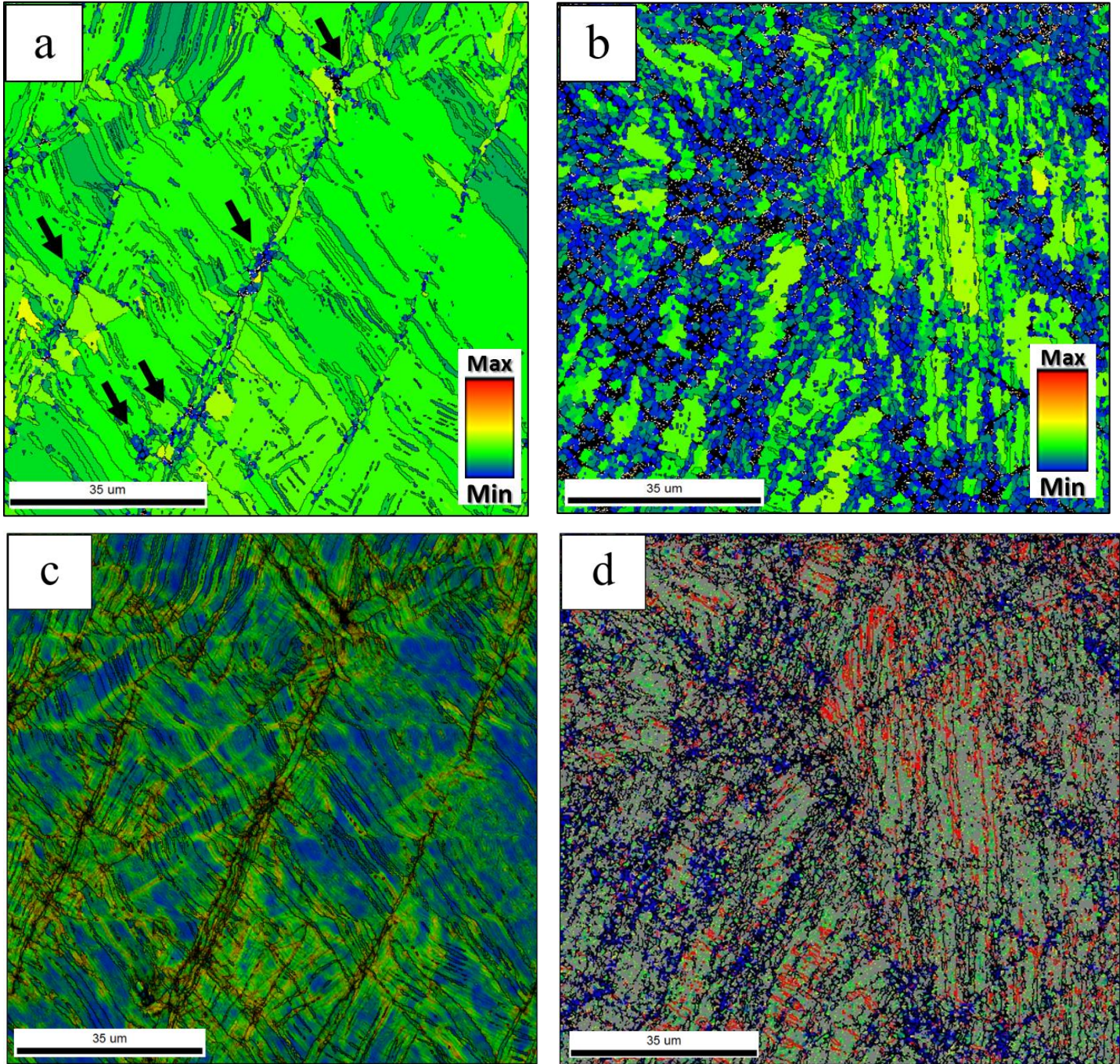


Fig.6. The grain average misorientation (GAM) maps after applying (a) one MAF pass ($\sum \varepsilon = 1.2$), and (b) two MAF passes ($\sum \varepsilon = 2.4$), the kernel average misorientation maps without and with superimposed grain boundaries in (c) one MAF pass condition, and (d) two MAF passes condition. The gray, black and red lines correspond to low-angle and high-angle boundaries with misorientation of $2^\circ < \Theta < 15^\circ$ and $\Theta > 15^\circ$, respectively and $\Sigma 3$ boundaries.

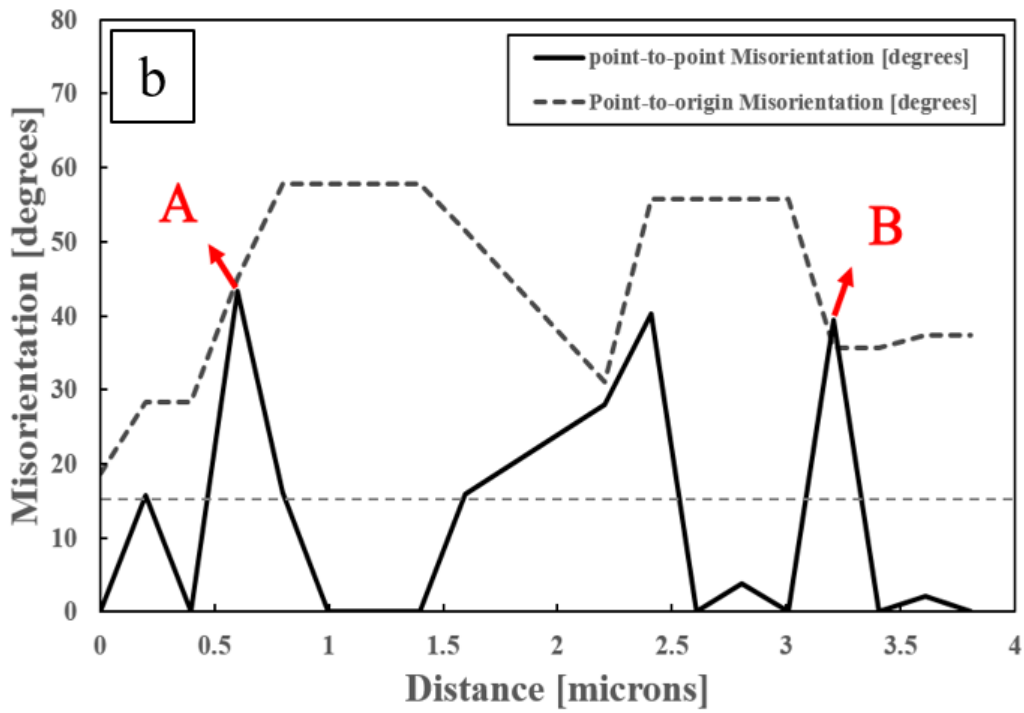
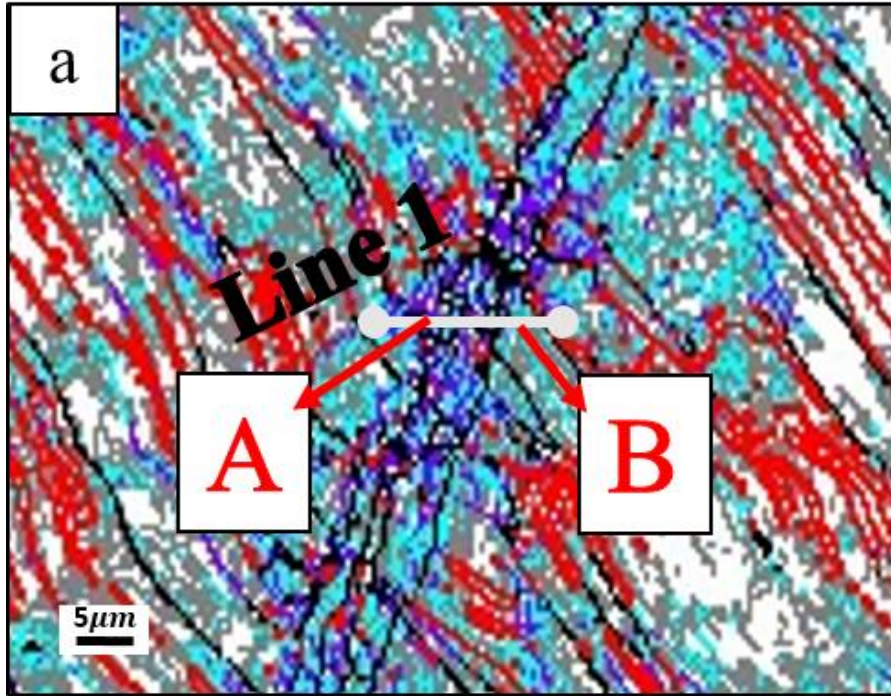


Fig. 7. (a) The selected area from the material after one MAF-pass processing and (b) the point to point and point to origin misorientation profiles along line 1.

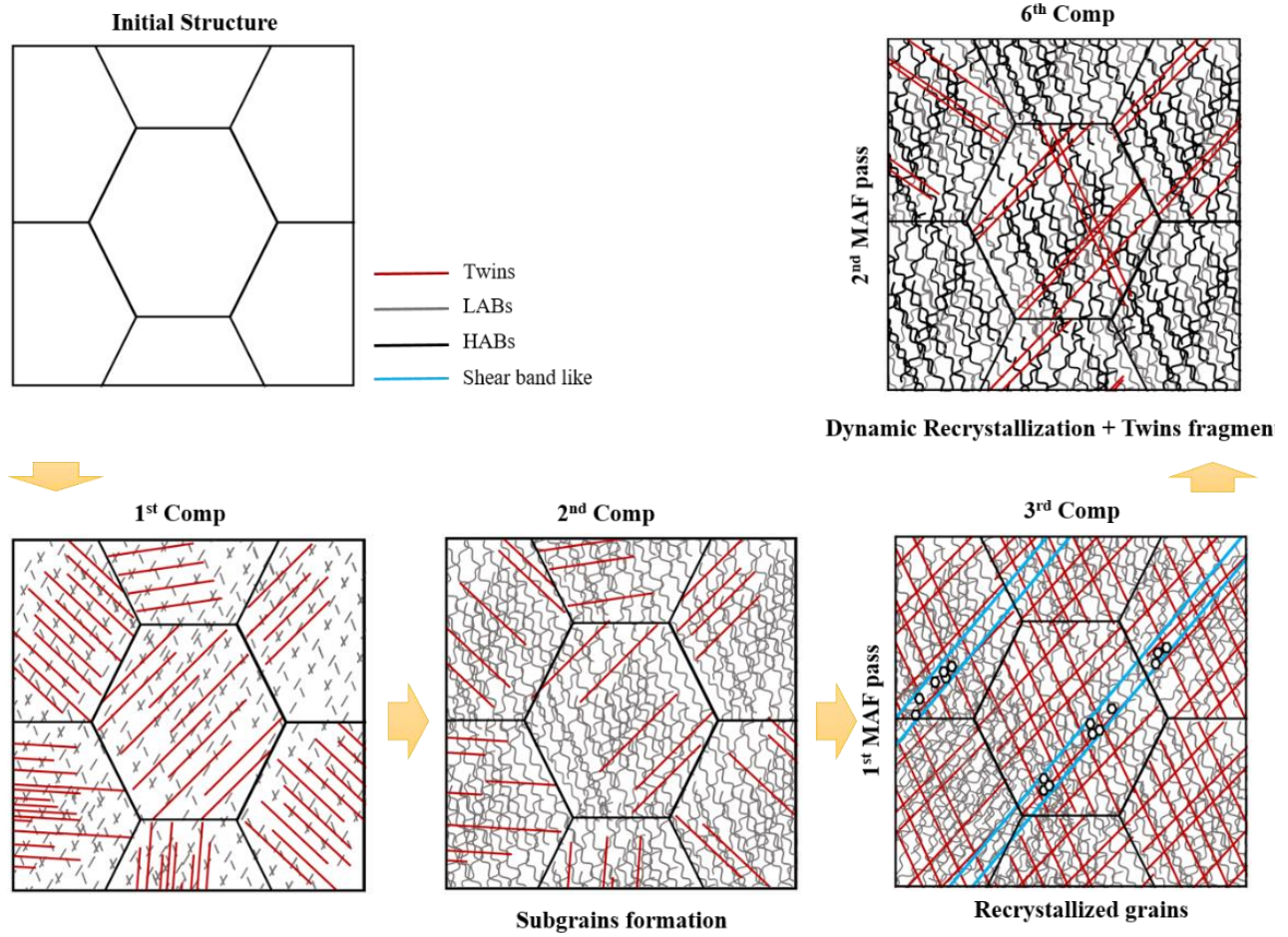


Fig. 8. Schematic representation of the grain refinement mechanism during MAF.

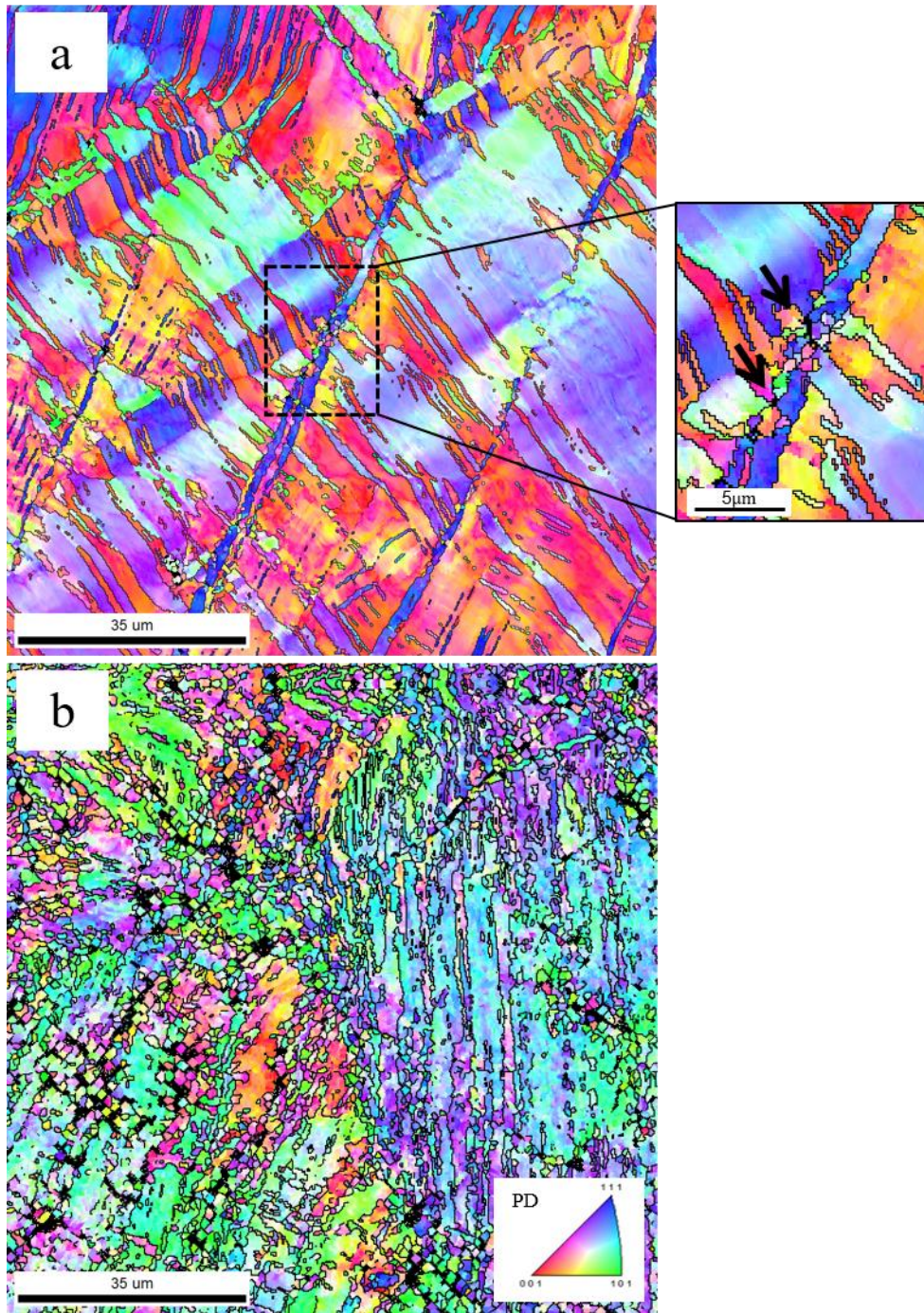


Fig. 9. The IPF maps from pressing direction (PD) of the processed materials after (a) one MAF pass, and (b) two MAF passes.

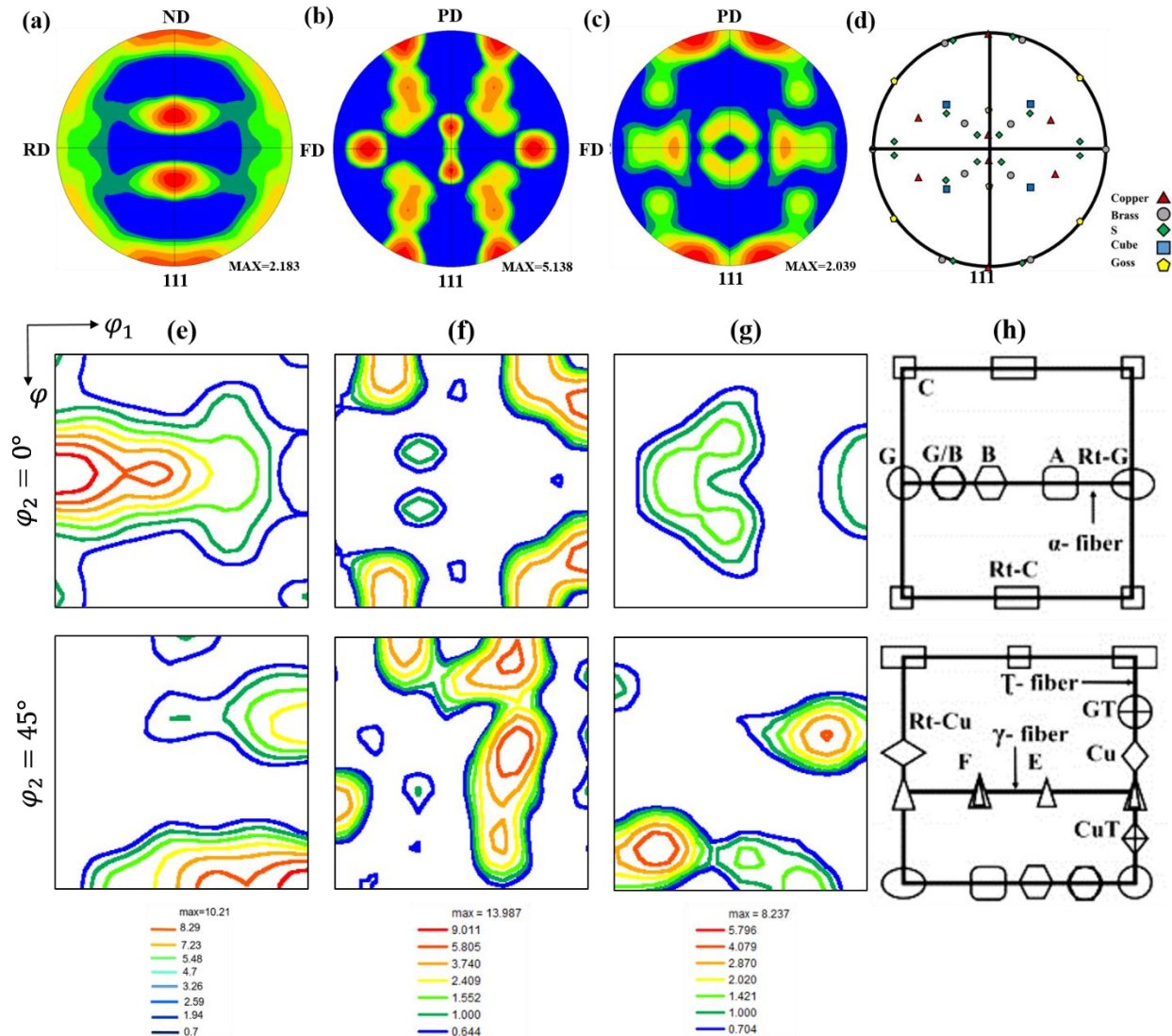


Fig.10. The $\{111\}$ pole figures and $\varphi_2 = 0^\circ$ and $\varphi_2 = 45^\circ$ ODF sections at different MAF passes: (a, e) initial, (b, f) one MAF pass and (c, g) two MAF passes. (d) Main ideal crystal orientations of a FCC material in (d) (111) pole figure and (h) ODF [26].

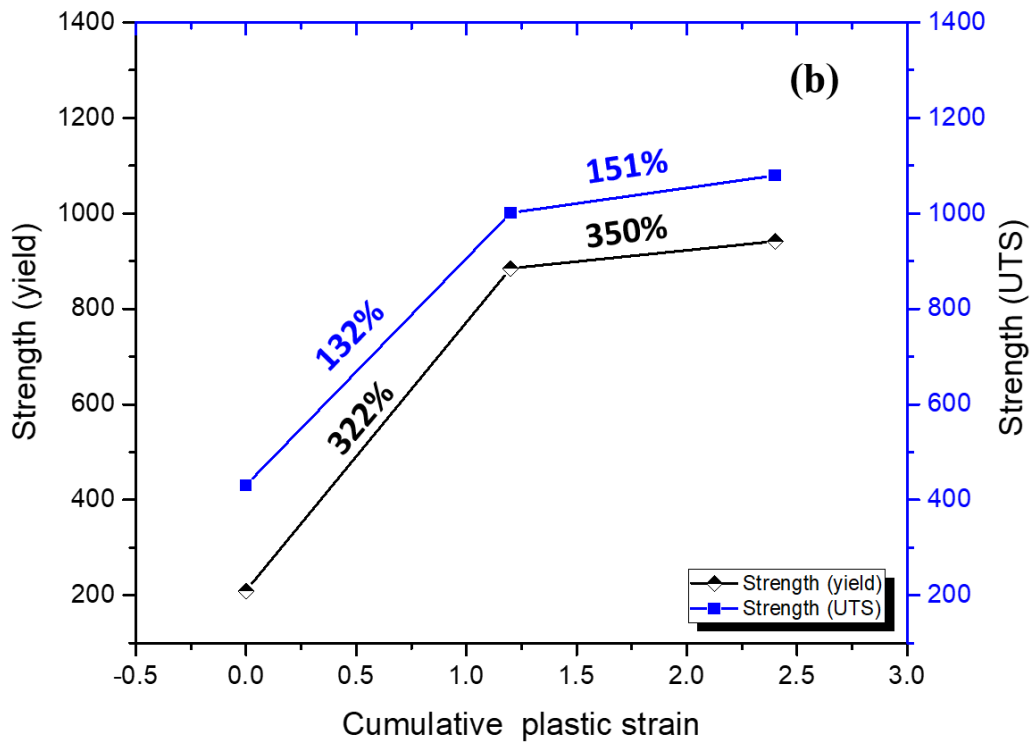
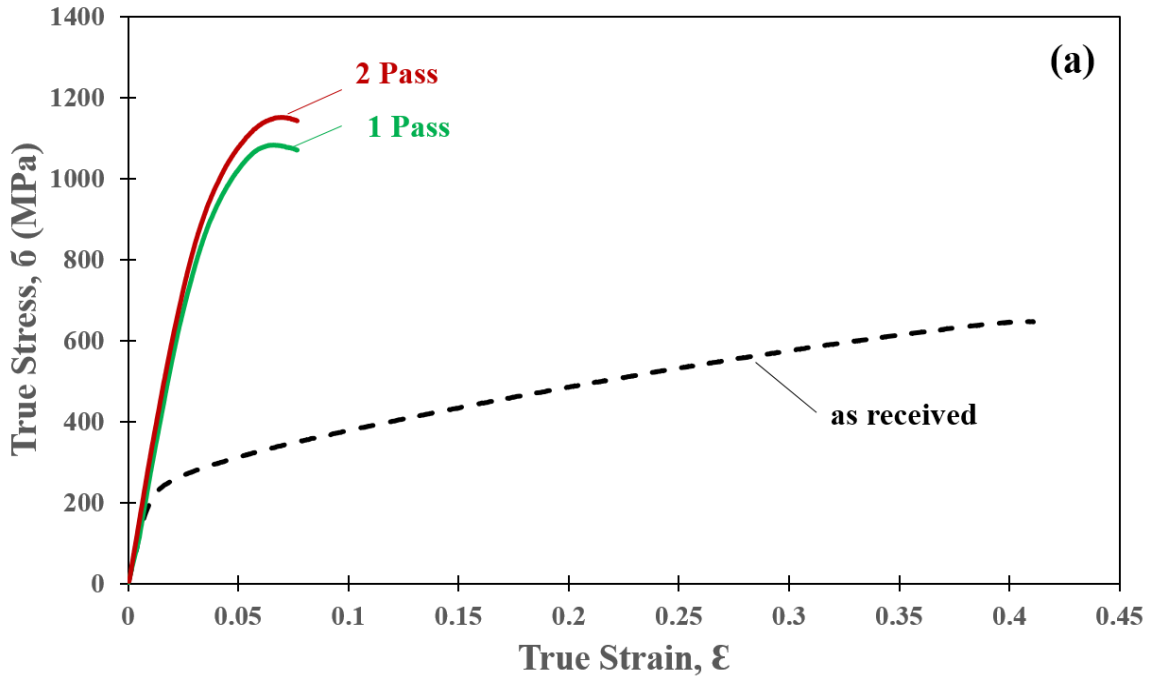


Fig.11. (a) the typical tensile flow behavior at room temperature, and (b) the evolution of yield strength and ultimate tensile strength by increasing the cumulative strain in experimented high Mn TWIP steel for as received and processed conditions.

Table.1. The chemical composition of experimental TWIP steel.

Chemical composition of the investigated steel							
Element	C	Mn	Al	Si	S	P	Fe
[Wt.%]	0.039	29.10	2.4	0.30	0.06	0.06	Bal.

Table.2. Comparison of the grain refinement mechanisms of austenitic steels.

Chemical composition (% wt.)	Mode of deformation	Strain path change	Each pass equivalent strain	Deformation temperature (k)	Dominant deformation mechanism	Twin suppression strain	Dominant grain refinement mechanism	Final strain	Ref.
Fe-23Mn-0.3C-1.5Al	Rolling	1	0.1(~10%)	300k	Dislocation slip+Twinning+ shear bands	0.51 (~40%r)	Grain fragmentation by twinning +crystallites formation within the shear bands	1.85(~80 %r)	[27]
Fe-0.3C-23Mn-1.5Al	Rolling	1	0.1(~10%)	293k	Dislocation slip+Twinning+ shear bands	0.92 (~60%r)	Grain fragmentation by twinning +crystallites formation within the shear bands	2.66(~93 %r)	[28]
Fe-0.3C-23Mn-1.5Al	Rolling	1	0.1(~10%)	77k	Dislocation slip+Twinning+ martensite formation +shear bands	0.51 (~40%r)	Grain fragmentation by twinning +crystallites formation within the shear bands	2.66(~93 %r)	[28]
Fe-24Mn-3Al-2Si-1Ni-0.06C	HPT	1	3.29	300k	Twinning+ small amount of martensite	1/4turn	Grain fragmentation by twinning	10turn	[15]
Fe-18Mn-0.75C-1.7Al-0.5Si	HPT	1	4.14	573k	Dislocation slip+small amount of twinning	1 turn	complex dislocation and GB activities	12 turn	[29]
Fe-23Mn-1.5Al-0.3C	ECAP	1	1.15	573k	Dislocation slip+small amount of nano Twins +micro band+ shear bands	1 pass	dislocation driven grain fragmentation+ fragmentation by twinning	4 pass	[49]
Fe-18.4Cr-8.1Ni-1.9Mn-1.3Si-0.03C-0.01S (ASS 304L stainless steel)	MAF	6	2.4	300k	martensite formation	-	Grain fragmentation by martensite	Failed at 2pass	[50]
				773k	dislocation driven slip+ deformation band	-	Continuous dynamic recrystallization (CDRX)	2pass	[50]
Fe-29.1Mn-2.4Al-0.3Si-0.06S-0.06P-0.04C	MAF	6	1.2	300k	Substructure development + Twinning +shear bands like	No suppression	Grain fragmentation by twinning + Continuous dynamic recrystallization	2pass	This work

Table.3. Mechanical properties of the material in different processing conditions. Initial, 1 pass and 2 pass of MAF, respectively.

Cumulative strain	Strength (yield)	Strength (UTS)	Total elongation (%)	UTS/YS
0	209.7	430.6	55.5	2.1
1.2	884.9	1000.6	9.5	1.1
2.4	941.7	1079.5	10.8	1.1

Fig. 1. The schematic representation of the applied multi-axial forging (MAF) method.

Fig. 2. (a) The inverse pole figure (IPF), and (b) the annealing twin map of the initial microstructure.

Fig. 3. The variation of true stress with cumulative strain during MAF of the experimental high Mn TWIP steel at room temperature.

Fig.4. The EBSD orientation maps illustrating the austenite grain boundaries at the interrupted strain of (a) 0.4, (b) 0.8, (c) 1.2 (1st MAF pass), and (d) 2.4 (2nd MAF pass). Gray, indigo, and purple lines holding misorientations in the range of $0.7^\circ < \Theta < 2^\circ$, $2^\circ < \Theta < 5^\circ$, and $5^\circ < \Theta < 15^\circ$, respectively. The black lines represent the high-angle grain boundaries having misorientation of $>15^\circ$. The red lines are $\Sigma 3$.

Fig. 5. The misorientation angle distributions in the microstructures of the workpieces deformed under different conditions of (a) $\sum \varepsilon = 0.4$, (b) $\sum \varepsilon = 0.8$, (c) $\sum \varepsilon = 1.2$, and (d) $\sum \varepsilon = 2.4$.

Fig.6. The grain average misorientation (GAM) maps after applying (a) one MAF pass ($\sum \varepsilon = 1.2$), and (b) two MAF passes ($\sum \varepsilon = 2.4$), the kernel average misorientation maps without and with superimposed grain boundaries in (c) one MAF pass condition, and (d) two MAF passes condition. The gray, black and red lines correspond to low-angle and high-angle boundaries with misorientation of $2^\circ < \Theta < 15^\circ$ and $\Theta > 15^\circ$, respectively and $\Sigma 3$ boundaries.

Fig. 7. (a) The selected area from the material after one MAF-pass processing and (b) the point to point and point to origin misorientation profiles along line 1.

Fig. 8. Schematic representation of the grain refinement mechanism during MAF.

Fig. 9. The IPF maps from pressing direction (PD) of the processed materials after (a) one MAF pass, and (b) two MAF passes.

Fig.10. The $\{111\}$ pole figures and $\varphi_2 = 0^\circ$ and $\varphi_2 = 45^\circ$ ODF sections at different MAF passes: (a, e) initial, (b, f) one MAF pass and (c, g) two MAF passes. (d) Main ideal crystal orientations of a FCC material in (d) (111) pole figure and (h) ODF ^[26].

Fig.11. (a) the typical tensile flow behavior at room temperature, and (b) the evolution of yield strength and ultimate tensile strength by increasing the cumulative strain in experimented high Mn TWIP steel for as received and processed conditions.

Table.1. The chemical composition of experimental TWIP steel.

Table.2. Comparison of the grain refinement mechanisms of austenitic steels.

Table.3. Mechanical properties of the material in different processing conditions. Initial, 1 pass and 2 pass of MAF, respectively.